Electrical transport and torque magnetometry studies of the kagome compound LuV_6Sn_6 under high magnetic fields

Cole Phillips,[1,*] Kyryl Shtefiienko,[1,*] Shirin Mozaffari,[2,*] Richa P. Madhogaria,[2] William R. Meier,[2] Aikaterini Flessa Savvidou,[3,4] Brian W. Casas,[3] Luis Balicas,[3,4] David G. Mandrus,[2,5] David E. Graf,[3,4] and Keshav Shrestha[1,†]

[1]*Department of Chemistry and Physics, West Texas A&M University, Canyon, Texas 79016, USA*
[2]*Department of Materials Sciences and Engineering, University of Tennessee, Knoxville, Tennessee 37996, USA*
[3]*National High Magnetic Field Laboratory, Tallahassee, Florida 32310, USA*
[4]*Department of Physics, Florida State University, Tallahassee, Florida 32306, USA*
[5]*Materials Science & Technology Division, Oak Ridge National Laboratory, Oak Ridge, Tennessee 37831, USA*

(Received 19 February 2025; revised 8 April 2025; accepted 10 April 2025; published 21 April 2025)

We present a comprehensive investigation of the kagome metal LuV_6Sn_6 through magnetotransport and torque magnetometry studies in magnetic fields up to 41 T and temperatures as low as 0.3 K. Magnetoresistance measurements up to 31 T reveal clear Shubnikov–de Haas (SdH) oscillations with two dominant frequency peaks: $F_\alpha = 12$ T and $F_\beta = 155$ T. The Berry phase $\Phi_\mathbf{B}$, calculated from Landau level fan diagrams, indicates a nontrivial topology for both the α- and β-orbits. To explore the possibility of higher-frequency signals in LuV_6Sn_6, we employed another technique: torque magnetometry. Torque measured with applied fields up to 41 T reveals clear de Haas–van Alphen (dHvA) oscillations, with frequency signals as high as 10 kT. Angular and temperature-dependent quantum oscillation measurements allowed us to extract the effective mass of charge carriers and map the Fermi surface of LuV_6Sn_6. To complement the experimental findings, we performed electronic band structure and Fermi surface calculations. The electronic bands of LuV_6Sn_6 reveal intriguing features, including flat bands, van Hove singularities, and Dirac points near the Fermi level. Two bands cross the Fermi level, contributing a deformed cylindrical shape at the Γ-point and small chainlike Fermi surfaces near the Brillouin zone boundaries. Theoretical quantum oscillation frequencies derived from Fermi surface cross-sectional areas align well with experimental SdH and dHvA results. These combined experimental and theoretical insights provide a deeper understanding of the electronic structure of LuV_6Sn_6 and establish the foundation for exploring electronic properties in other vanadium- and titanium-based kagome systems.

DOI: 10.1103/PhysRevB.111.155136

I. INTRODUCTION

Kagome materials have recently gained significant attention in research due to their rich and intriguing properties, such as superconductivity, nontrivial topology, charge density wave (CDW), and frustrated magnetism [1–3]. Their quasi-two-dimensional lattice structure resembles the traditional Japanese basket-weaving pattern [2]. A notable example is the vanadium-based AV_3Sb_5 (A = K, Rb, Cs) family [4,5], also known as the 135 family, which forms a hexagonal lattice of vanadium atoms coordinated by antimony atoms. These materials exhibit a variety of exotic quantum phenomena, such as superconductivity with critical temperature (T_c) between 0.3 and 3 K, CDW order near $T_{CDW} \sim 80$–110 K, and nontrivial topological features, including multiple Dirac and van Hove singularities near the Fermi level [6–9]. The coexistence of nontrivial topology and superconductivity makes the 135 family a promising platform for exploring topological superconductivity and Majorana fermions [10]. Several studies under high magnetic fields on this family were carried out to understand their Fermi surface properties [11–14]. Our recent high-pressure studies [15] under high magnetic fields have revealed that the Fermi surface of CsV_3Sb_5 undergoes reconstruction at pressures above 0.7 GPa.

Beyond the 135 family, several new vanadium- and titanium-based kagome materials, such as RV_6Sn_6 (R = rare earth) [16–20] and ATi_3Bi_5 [21–23], have been discovered. These compounds feature corner-sharing kagome layers of vanadium or titanium atoms. In the RV_6Sn_6 family, GdV_6Sn_6, HoV_6Sn_6, and YV_6Sn_6 have exhibited topological properties [18,24]. Notably, ScV_6Sn_6 remains the only member of this family to display CDW order, below $T_{CDW} = 92$ K [25], without any observed superconductivity under ambient conditions or pressures up to 11 GPa [26]. In the titanium-based ATi_3Bi_5, which is isostructural to AV_3Sb_5, neither superconductivity nor CDW phases have been observed. However, quantum oscillation measurements have hinted at their nontrivial topological properties [22,27]. Recently, Ortiz *et al.* [28,29] reported another titanium-based family, $LnTi_3Bi_4$ (Ln = lanthanides), which crystallizes in an orthorhombic structure ($Fmmm$, no. 69). Unlike previous kagome families, $LnTi_3Bi_4$ features slightly distorted kagome lattices and zigzag Ln

*These authors contributed equally to this work.
†Contact author: kshrestha@wtamu.edu

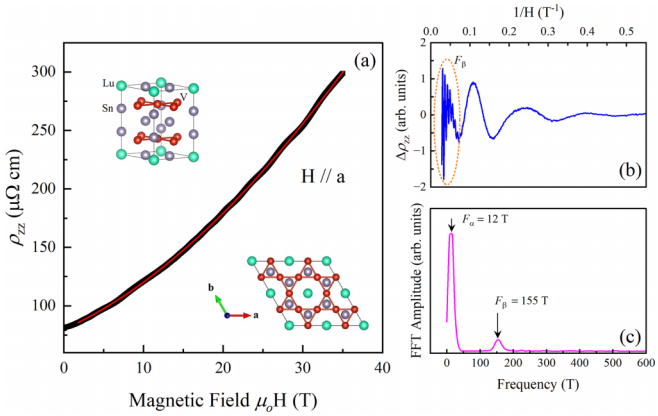

FIG. 1. (a) Magnetic field dependence of the electrical resistivity, ρ_{zz}, for LuV_6Sn_6 at $T = 1.3$ K and $\theta = 0°$. The $\rho_{zz}(H)$ curve exhibits distinct Shubnikov–de Haas (SdH) oscillations above 5 T. The red curve represents a third-order polynomial fit to the data. Upper inset: Crystal structure of LuV_6Sn_6, highlighting the unit cell. Lower inset: kagome lattice formed by V-atoms. (b) Background-subtracted ρ_{zz} data, revealing SdH oscillations corresponding to two distinct periods. (c) Frequency spectrum of the SdH oscillations, showing two dominant frequencies: $F_\alpha = 12$ T and $F_\beta = 155$ T.

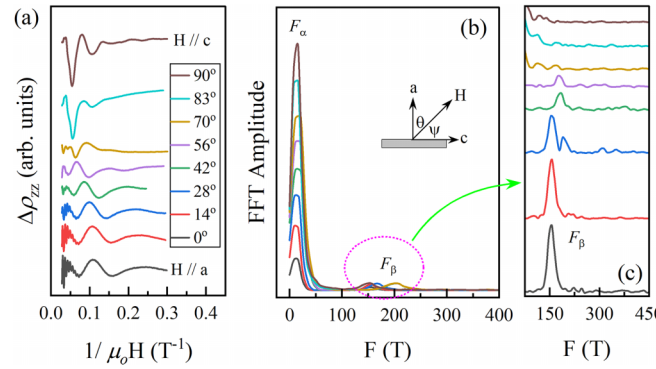

FIG. 2. (a) Background-subtracted resistivity ($\Delta\rho_{zz}$) data for LuV_6Sn_6 at different θ values. The SdH oscillations are clearly visible at all measured angles. Both low- and high-frequency signals are present at $\theta = 0°$, while the high-frequency signal appears to disappear above 70°. (b) The frequency spectra for the SdH oscillations shown in (a). There are two frequency peaks, F_α and F_β, in the spectrum. Inset: The tilt angle θ, defined as the angle between the c-axis and the magnetic field direction H. (c) A zoomed-in frequency spectrum highlighting F_β. The F_β peak shifts to higher values with increasing θ and becomes indistinguishable above 56°. The curves in (a), (b), and (c) are shifted for clarity.

chains embedded within *Ln*-Bi bilayers. Our recent high-field torque magnetometry studies [30] on $YbTi_3Bi_4$, along with density functional theory (DFT) calculations, showed the presence of multiple quasi-two-dimensional Fermi surfaces in this material.

This study focuses on the electronic structure of LuV_6Sn_6 through high-field magnetotransport and torque magnetometry up to 41 T. LuV_6Sn_6, a member of the RV_6Sn_6 family, crystallizes in the $P6/mmm$ space group [17,31]. The unit cell and kagome layer of vanadium atoms are depicted in the insets of Fig. 1(a). Our transport and magnetization measurements [31] show no evidence of CDW or magnetic or superconducting orders. Although extensive research has been conducted on other members of the RV_6Sn_6 family, studies on LuV_6Sn_6 through high-field magnetotransport or torque magnetometry remain scarce. This work combines results from magnetoresistance and torque measurements to explore its electronic structure. Quantum oscillations are clearly observed in both magnetoresistance and torque data, with multiple frequencies as high as 10 kT. Additionally, electronic band structures and the Fermi surface were computed using density functional theory to explain the experimental observations. Our DFT results are in good agreement with the experimental findings.

II. EXPERIMENTAL AND COMPUTATIONAL DETAILS

LuV_6Sn_6 samples were synthesized via the tin flux method following the procedure outlined in Refs. [31,32]. Elemental Lu (Alfa Aesar, 99.9%), V (Alfa Aesar, 99.8%), and Sn (Alfa Aesar, 99.9999%) were placed inside an alumina Canfield crucible set, which was then sealed in a silica ampoule filled with approximately 0.2 atm of argon. The ampoule was heated to 1150 °C over 12 h, held at that temperature for 15 h, and then cooled to 780 °C over 300 h. To remove the tin flux, the ampoule was centrifuged at 780 °C. Residual tin on the surface of the crystals was removed by etching in an aqueous 10 wt. % HCl solution for 12–16 h.

Magnetotransport and torque magnetometry measurements were conducted at the National High Magnetic Field Laboratory (NHMFL) in Tallahassee, FL, using resistive magnets with a top-loading ^{3}He cryostat. Resistivity measurements were carried out using the standard four-wire configuration, whereas torque measurements were performed using a miniature piezoresistive cantilever. The sample was rotated *in situ* in applied fields at various tilt angles (θ), where θ is the angle between the magnetic field and the a-axis of the sample, as shown in Fig. 2(b), inset. Magnetic fields were swept at each fixed temperature at a rate of 1.5 T/min.

The electronic structure calculations were performed using density functional theory (DFT) within the full-potential linearized augmented plane wave (FP-LAPW) method, as implemented in the WIEN2K code [33]. Exchange-correlation energies were treated using the Perdew-Burke-Ernzerhof generalized gradient approximation (PBE-GGA) [34]. Atomic coordinates were optimized in the scalar relativistic mode until the forces on individual atoms were reduced below 20 meV/Å. Spin-orbit coupling (SOC) was incorporated via the second-variational approach [35]. The self-consistent calculations were conducted with an energy convergence criterion of 10^{-4} Ry. Atomic sphere radii Radius Muffin-Tin (RMT) were set to 2.50 Bohr for Lu, V, and Sn. A grid of 800 k-points was used for self-consistent calculations across the full Brillouin zone, while a finer grid of 9000 k-points was employed for Fermi surface computations.

III. RESULTS AND DISCUSSION

Figure 1(a) shows the electrical resistivity (ρ_{zz}) of the LuV_6Sn6 single crystal as a function of the magnetic field (H). Here, the current is applied along the c-axis, and ρ_{zz}

represents the resistivity along the c-axis. The ρ_{zz} (H) increases with magnetic field, showing a positive magnetoresistance (MR). The MR value, calculated using the formula $\mathrm{MR} = [\rho_{zz}(H) - \rho_{zz}(0)]/\rho_{zz}(0)$, where ρ_{zz} (H) and ρ_{zz} (0) are the resistivity values at the fields H and 0, respectively, is found to be 275%. This MR value is five times higher than that of another member, YV_6Sn_6, in the same magnetic field range [36]. At high fields above 5 T, ρ_{zz} (H) displays an oscillation-like feature, known as Shubnikov–de Haas (SdH) oscillation [37,38]. The SdH oscillations in resistivity of metals arise due to the quantization of electron energy levels, known as Landau levels, in the presence of a strong magnetic field. To extract the SdH signal, we carried out background subtraction by fitting the data with a third-order polynomial, as indicated by the red curve. The background-subtracted oscillation is depicted in Fig. 1(b). As seen in the graph, there are two distinct periods, indicating the presence of two frequency components. The high-frequency signal appears at higher fields above 10 T, as indicated by the dotted area. Figure 1(c) shows the frequency spectrum of the data shown in Fig. 1(b). There are two major frequency peaks at $F_\alpha = 12\,\mathrm{T}$ and $F_\beta = 155\,\mathrm{T}$.

Quantum oscillations in metals under high magnetic fields occur due to the quantization of electronic states into Landau levels [37]. Physical properties such as electrical resistivity (or conductivity) and magnetization, which depend on the electronic density of states, become periodic functions of the magnetic field [37,38]. The oscillations in conductivity and magnetization are known as SdH and dHvA (de Haas–van Alphen) oscillations, respectively. According to Onsager's relation [39], the frequency (F) of these quantum oscillations is directly proportional to the cross-sectional area of the Fermi surface (A_F), given by $F = \frac{\hbar}{2\pi e} A_F$, where $\hbar$ is the reduced Planck's constant, and e is the electron charge. Therefore, by rotating the sample in magnetic field, it is possible to map the Fermi surface cross-sections at different angles and hence we can map the Fermi surface of a material under study. For mapping the Fermi surface of LuV_6Sn_6, we measured magnetoresistance by rotating the sample at different tilt angles θ, as presented in Fig. S1 in the Supplemental Material (SM) [40].

The background-subtracted magnetoresistance data at selected tilt angles θ are presented in Fig. 2(a), with vertical shifts applied for better visualization. The periods of SdH oscillations change with θ, indicating a shift in frequency values with θ. This is more clearly seen in the frequency plots in Figs. 2(b) and 2(c). The low-frequency signal F_α near 10 T is consistently observed across all measured angles (0° to 90°), with its position remaining nearly unchanged. In contrast, the high-frequency signal F_β gradually shifts to higher values, and its amplitude diminishes at larger θ. F_β becomes indistinguishable above 56°, as shown in Fig. 2(c). The angular dependence of F_α and F_β is analyzed and later compared with theoretical results.

To investigate the topological nature of LuV_6Sn_6, the Berry phase $\Phi_\mathbf{B}$ was calculated using the Landau level (LL) fan diagram [38]. In topologically trivial systems, $\Phi_\mathbf{B}$ equals 0, whereas in topologically nontrivial systems, $\Phi_\mathbf{B}$ equals π [41–43]. Due to the presence of two frequency signals (Figs. 1 and 2), assigning LL indices and constructing the LL fan plot was challenging. Therefore, band-pass FFT filters were applied to the raw data to isolate the SdH oscillations corresponding to F_α and F_β. This approach has been successfully used in Berry phase studies of other topological and kagome materials [20,43,44]. Figure 3(a) shows the background-subtracted resistivity data for LuV_6Sn_6 (green curve), while the blue and black curves represent the SdH oscillations filtered for 2–22 and 70–300 T ranges, respectively. The single peaks at 10 and 155 T, as seen in the inset, confirm that the filtered SdH oscillations correspond solely to F_α and F_β.

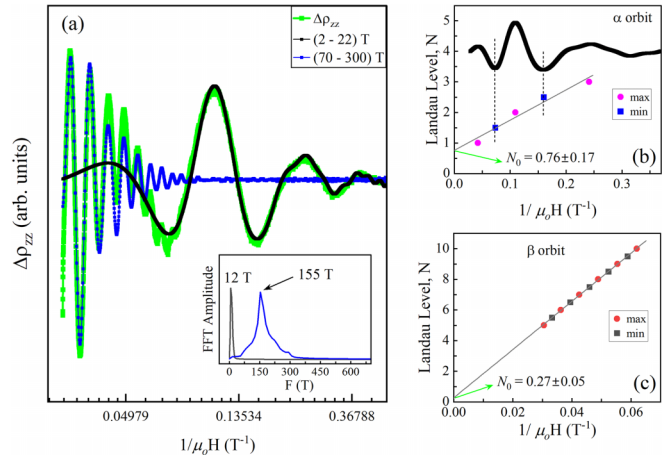

FIG. 3. (a) Background-subtracted resistivity $(\Delta\rho_{zz})$ data for LuV_6Sn_6 at $\theta = 0°$. The black and blue curves represent the filtered signals obtained using fast Fourier transform (FFT) band-pass filters in the ranges of 2–22 and 70–300 T, respectively. Inset: FFT spectrum of the filtered oscillations, confirming the presence of a single frequency. (b),(c) Landau level fan plots for the α- and β-orbits, respectively. Data points are shown as squares and circles, with dashed lines representing linear extrapolations.

Figures 3(b) and 3(c) present the LL fan diagrams for the α- and β-orbits, respectively. According to Ando [38], the minima and maxima of the conductivity are assigned integer and half-integer values, respectively, when constructing the LL fan plot. The conductivity is given by $\sigma_{zz} = \rho_{zz}/(\rho_{zz}^2 + \rho_{yz}^2)$. Since the Hall component ρ_{yz} is very small compared to the longitudinal component ρ_{zz}, as demonstrated in our recent report on LuV_6Sn_6 [31], it follows that $\sigma_{zz} \sim 1/\rho_{zz}$. Therefore, we have assigned integer and half-integer indices to the maxima and minima of the SdH oscillations, respectively. As seen in the LL fan plot, the α-orbit reaches the quantum limit under the application of a 41 T magnetic field. The linear extrapolation in the limit of $1/H \to 0$ yielded intercept values of $N_0 = 0.76$ and 0.27 for the α- and β-orbits, respectively. These N_0 correspond to Berry phase values of $(1.52 \pm 0.34)\pi$ and $(0.54 \pm 0.10)\pi$. The nonzero Berry phase for the both α- and β-orbits indicates their nontrivial topological property [38]. It is important to note that the nontrivial topological feature of the frequency peak near 10.8 T in LuV_6Sn_6, observed using torque magnetometry, has also been reported [45], which is consistent with our results here. Furthermore, the slope of linear extrapolation yielded (9.89 ± 1.18) and (157.47 ± 1.05) T for the α- and β-orbits, respectively. These values are in good agreement with F_α and F_β at $\theta = 0°$ [Fig. 1(c)], confirming that the FFT filtered signal preserves the original signal without introducing artifacts.

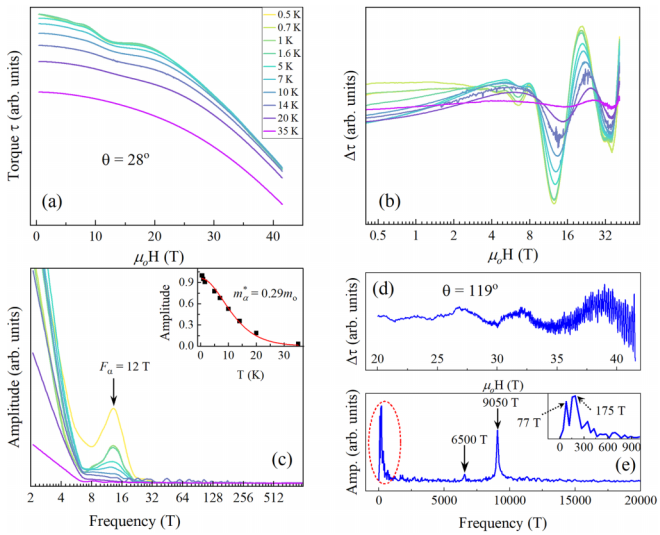

FIG. 4. (a) Torque (τ) data of LuV_6Sn_6 single crystal at different temperatures under applied magnetic fields up to 41 T. (b) Background-subtracted torque data ($\Delta\tau$) for the data shown in (a). The $\Delta\tau$ (H) show clear de Haas–van Alphen (dHvA) oscillations above 4 T. (c) Frequency spectra at different temperatures, indicating a single dominant frequency at 12 T. Inset: Lifshitz-Kosevich analysis of the temperature-dependent quantum oscillation data, with the solid curve representing the best-fit model. The x-axes in (b) and (c) are presented on a logarithmic scale for better visibility. (d) $\Delta\tau(H)$ data at $\theta = 119°$, showing both high- and low-frequency dHvA oscillations. (e) Frequency spectrum corresponding to the data in (d), revealing high-frequency signals around 6 and 9 kT, along with low-frequency components. Inset: Frequency spectrum in the low-frequency region (dotted area), highlighting two peaks near 77 and 175 T.

In our magnetotransport measurements on LuV_6Sn_6 under applied fields up to 35 T, we observed distinct SdH oscillations with frequencies of 12 and 154 T. However, we did not find any evidence of higher-frequency signals in the kilotesla range within our magnetotransport data, as previously reported for related compounds ScV_6Sn_6 and YV_6Sn_6 [20,46]. Furthermore, theoretical frequencies from our DFT calculations predict the possibility of high frequencies on the order of 8–10 kT for LuV_6Sn_6. To further investigate this possibility, we employed torque magnetometry as an alternative method for studying quantum oscillations.

Figure 4(a) displays the torque (τ) data for LuV_6Sn_6 with maximum applied fields up to 41 T at various temperatures. There is clear evidence of dHvA oscillations in the $\tau(H)$ data. The oscillations gradually diminish at higher temperatures. This feature is more evident in the background-subtracted data shown in Fig. 4(b). However, the frequency spectrum of the dHvA oscillations reveals the presence of only a single peak near 12 T. This value is in good agreement with the F_α signal observed in the SdH data (Figs. 1 and 2). The amplitude of the frequency peak decreases with increasing temperature. This behavior can be described by the Lifshitz-Kosevich (LK) formula [38,47,48]. According to LK theory, the temperature and magnetic field dependence of quantum oscillations are given by

$$\Delta\tau(T,H) \propto e^{-\lambda_D}\frac{\lambda(T/H)}{\sinh[\lambda(T/H)]}, \tag{1}$$

with $\lambda_D(H) = \frac{2\pi^2 k_B}{\hbar e} m^* \frac{T_D}{H}$ and $\lambda(T/H) = \frac{2\pi^2 k_B}{\hbar e} m^* \frac{T}{H}$. Here, T_D, k_B, and m^* represent the Dingle temperature, Boltzmann's constant, and effective mass of the charge carriers, respectively. The first term is the Dingle factor, which describes the attenuation of the oscillations with decreasing field H. The second term explains the weakening of the oscillations at higher temperatures.

We have plotted the variation of frequency amplitude with temperature, as shown in the inset of Fig. 4(c). The red curve represents the best fit to the data using the LK formula. As seen in the graph, the LK theory accurately describes the temperature dependence of the SdH data. From the best-fit curve, we determined the effective mass $m^*_\alpha = 0.29m_o$ for the α-orbit, where m_o is the free-electron mass. This value is in close agreement with the effective mass reported for ScV_6Sn_6 and YV_6Sn_6 [20,46].

In our torque data (Fig. 4), we observed a single peak at 12 T, which aligns with the F_α in the magnetoresistance data (Fig. 1). Berry phase analysis of the α-orbit, determined by constructing the Landau level fan plot from SdH oscillations, reveals a nontrivial topological feature, as shown in Fig. 3(b). To validate this result, we calculated the Berry phase using the dHvA oscillations from the torque data, presented in Fig. S3 of the SM [40]. From the linear extrapolation of the data, we obtained $\Phi_\mathbf{B} = (0.70 \pm 0.22)\pi$, which further supports the nontrivial topology of the α-orbit.

It is important to note that the torque data taken at $\theta = 28°$ in Fig. 4(a) show the presence of only the low frequency near 12 T, however there is no signature of high frequencies. To investigate the high-frequency signal, we rotated the sample at different tilt angles and we could resolve high-frequency signals of the order of 8–10 kiloteslas at some angles. For example, Fig. 4(d) shows the background-subtracted torque data at $\theta = 119°$. As seen in the graph, there is modulation of more than one frequency signal, which is clarified in the frequency spectrum in Fig. 4(e). The frequency spectrum shows the presence of two high-frequency signals around 6.5 and 9 kT, along with a low-frequency peak. The inset shows the zoomed-in spectrum in the low-frequency region, highlighting two peaks near 77 and 175 T. The SdH data also exhibit a peak $F_\beta \sim 155$ T at $\theta = 0°$, which is comparable to the 175 T peak in the dHvA data. The higher value of 175 T in the dHvA data is due to measurements taken at a different tilt angle, $\theta = 119°$.

The angular variation of the torque signal with applied fields up to 41 T is presented in Fig. S2 of the SM [40]. The dHvA oscillations are clearly observed at all measured angles. The low-frequency signal F_α is dominant and present at all measured angles, whereas the high-frequency signal, on the order of 8–10 kT, is weak and observed only in the high magnetic field region (above 35 T) and at certain angles. For example, the frequency peak near 9.5 kT is clearly observed at 56°, but it is not well resolved at 42°. Such behavior has also been observed in previous torque data for other compounds, ScV_6Sn_6 and YV_6Sn_6, from the same family [20,46]. Therefore, increasing the magnetic field range

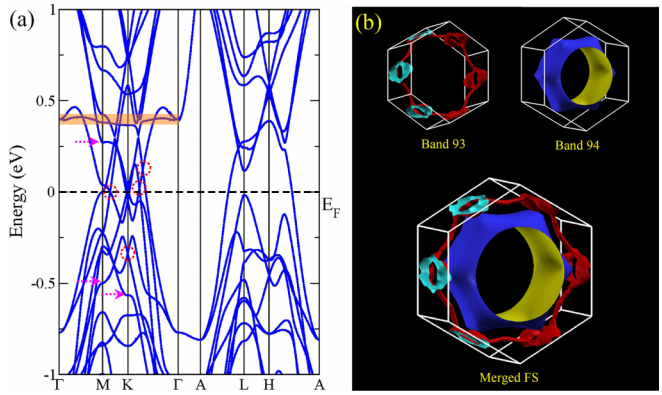

FIG. 5. (a) Electronic band structure of LuV_6Sn_6 along high-symmetry k-points without including spin-orbit coupling. The band structure exhibits notable features such as flat bands, van Hove singularities, and Dirac points near the Fermi level, highlighted by the shaded area, arrows, and dotted circles, respectively. (b) Fermi surfaces corresponding to bands 93 and 94 (upper panels) and the combined Fermi surface of LuV_6Sn_6. The Fermi surface of band 93 forms a ringlike structure at the boundary, while that of band 94 appears as a deformed cylindrical shape with a bulging center around the Γ-point.

above 41 T might be useful for studying the angle-dependent behavior of the high-frequency signal and identifying its origin.

To support our experimental observation, we computed the electronic bands and Fermi surface of LuV_6Sn_6 using the density functional theory. Figure 5(a) shows the electronic bands of LuV_6Sn_6 along the high symmetry points in the Brillouin zone. As seen in the figure, there are several interesting features: Dirac points, a flat band, and van Hove singularity points near the Fermi level, as indicated by the dotted circles, shaded area, and dashed arrows, respectively. Two bands (Band 93 and Band 94) cross the Fermi level and they contribute to the Fermi surface of this material. The Fermi surface of Band 93 is a hexagonal chainlike feature at the boundary of the Brillouin zone, whereas that of Band 94 has a deformed cylindrical-like feature with a belly at the center, and it is centered at the Γ-point. These features of the band structure and Fermi surface are consistent with those of other kagome materials [16,20,46].

According to the Onsager relation [39], the frequency of quantum oscillations is directly proportional to the cross-sectional area of the Fermi surface. Thus, we can calculate the theoretical frequencies by analyzing the Fermi surface of Bands 93 and 94. We used the SKEAF code [49] to compute these theoretical frequencies, which are presented in Fig. 6. For comparison, we also include frequencies derived from magnetoresistance and torque measurements. The theoretical frequencies from Band 93, along with their angular variations, are shown in Fig. 6(a). Three potential frequencies are identified: 14, 85, and 290 T. The low-frequency value of 14 T aligns well with F_α observed in both SdH and dHvA oscillations. However, no experimental frequencies near 85 or 290 T were observed, despite predictions from DFT calculations. To improve the comparison, we raised the Fermi level by 25 meV. This adjustment, while somewhat ad hoc, simulates the effect of doping, as the exact experimental Fermi level is often uncertain. The Fermi surface of Band 93, with the chemical potential shifted by +25 meV, is shown in Fig. S4 in the SM [40]. The ringlike feature disappears with this shift. The frequency derived after shifting the Fermi level is shown in the inset, where the theoretical frequency now aligns closely with F_β observed in SdH oscillations.

The Fermi surface associated with Band 94 exhibits a deformed cylindrical shape with multiple cross-sectional areas

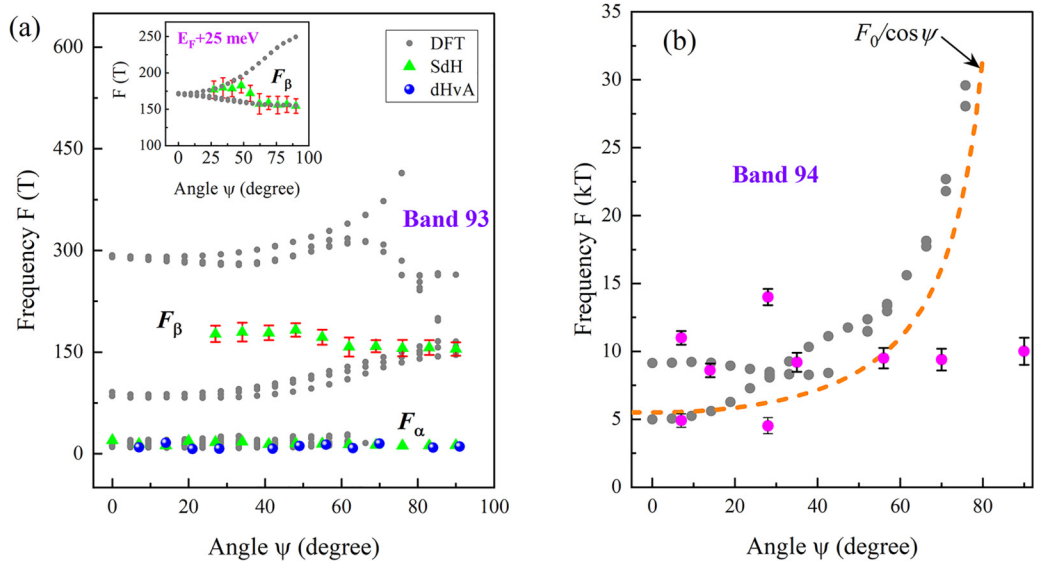

FIG. 6. (a) Comparison of experimental frequencies (F_α and F_β) with DFT-computed theoretical frequencies from the Fermi surface of Band 93. Inset: Theoretical frequencies with a 25 meV Fermi level shift, showing that F_β aligns well with the theoretical values. (b) DFT-derived frequencies from the Fermi surface of Band 94. These frequencies are on the order of kiloteslas and closely follow a $1/\cos\psi$ trend (dashed curve), as expected for a cylindrical Fermi surface. Experimental frequencies are also on the kilotesla scale and are comparable to theoretical values, particularly at low tilt angles.

[Fig. 5(b)]. The theoretical frequencies derived from Band 94 are shown in Fig. 6(b). As indicated by the dashed curve, the theoretical frequencies follow a nearly $1/\cos\psi$ angular variation, consistent with a cylindrical Fermi surface. Here, ψ is the angle between the magnetic field direction and the c-axis, as depicted in the inset of Fig. 2(b). Theoretical calculations using SKEAF show possible frequencies around 5 and 9 kT. To check for the presence of high-frequency signals in our torque data, we conducted careful analyses in the high magnetic field region, as presented in Fig. S2 in the SM [40]. We also observed high-frequency peaks near 5 and 10 kT, indicated by the pink circles in our torque data. However, these signals are only observed above 35 T and at specific angles, making a direct one-to-one mapping between the experimental and DFT data challenging. Extending the magnetic field range beyond the current maximum of 41 T could help better resolve these high-frequency signals and improve comparisons with DFT predictions.

It is worth noting that in the high-field (low $1/H$) region of Fig. 3(b) (also in Fig. S3 in the SM), the amplitude of the quantum oscillations exhibits a noticeable decay. As shown in the figure, the SKEAF output indicates the presence of multiple low-frequency orbits near the Fermi level, which could lead to interference effects and potentially contribute to deviations from an ideal sinusoidal behavior. While the FFT of the SdH oscillations reveals a dominant frequency $\sim$12 T, subtle contributions from nearby orbits cannot be entirely ruled out and may slightly influence the observed phase and amplitude. Further high-resolution measurements may help resolve these closely spaced frequencies. In addition, the effective masses m^* derived from the SKEAF output of band 93 are presented in Fig. S5 in the SM [40]. The m^* is $\sim 0.23m_o$ for the α-orbit, which is comparable to the value of $0.29m_o$ derived from the LK fit in Fig. 4.

IV. SUMMARY

The 166-kagome family RV_6Sn_6 (R = rare-earth) is predominantly magnetic due to the magnetic moments of the rare-earth elements. However, only a few compounds, such as ScV_6Sn_6, YV_6Sn_6, and LuV_6Sn_6, have been identified as nonmagnetic. Among them, LuV_6Sn_6 is particularly notable for its clean, nonmagnetic nature, making it an excellent candidate for studying the topological properties of the kagome lattice without the interference of magnetic effects. In this study, we present a comprehensive study of the kagome metal LuV_6Sn_6 through systematic electrical transport and torque magnetometry measurements under high magnetic fields up to 41 T. Magnetoresistance measurements reveal distinct Shubnikov–de Haas (SdH) oscillations with two prominent frequency peaks at $F_\alpha = 12$ T and $F_\beta = 155$ T. Similarly, torque magnetometry data exhibit clear de Haas–van Alphen (dHvA) oscillations, including a low-frequency peak at 12 T and a high-frequency signal around 10 kT. Notably, this high-frequency signal emerges only at magnetic fields above 35 T and is observed only in specific field directions.

Temperature-dependent quantum oscillation measurements, analyzed using the Lifshitz-Kosevich formalism, provide effective-mass estimates for charge carriers. Additionally, angle-dependent measurements allow us to map the Fermi surface of LuV_6Sn_6. To probe its topological character, we calculate the Berry phase by constructing the Landau level fan plot, revealing nontrivial topology associated with the α- and β-orbits. To complement our experimental findings, we perform electronic band structure and Fermi surface calculations. The band structure of LuV_6Sn_6 exhibits key features such as flat bands, van Hove singularities, and Dirac points near the Fermi level. Two bands contribute to the Fermi surface, consisting of a deformed cylindrical surface centered at the Γ-point and a smaller surface at the Brillouin zone boundaries. Importantly, theoretical frequencies derived from Fermi surface cross-sectional areas show strong agreement with experimental SdH and dHvA results.

It is important to note that the magnetoresistance data in our experiment do not exhibit the signature of a high-frequency signal originating from the cylindrical Fermi surface of Band 94. In contrast, the torque data reveal a high-frequency signal in the range of 8–10 kT. This discrepancy may arise because electron transport is governed by scattering mechanisms, causing SdH oscillations in magnetoresistance to be affected by various scattering processes in the sample. On the other hand, dHvA oscillations originate directly from the electrons' free energy, and the torque technique is more sensitive to quantum oscillation signals. The high-frequency signal in our data is weak and overshadowed by the dominant low-frequency signal, appearing only at specific tilt angles, which complicates the direct comparison with theoretical values computed by DFT. Increasing the magnetic field beyond the current limit of 41 T could be a potential approach to further investigate the fermiology of this high-frequency signal in LuV_6Sn_6. This combined experimental and theoretical study provides a detailed understanding of the electronic structure of LuV_6Sn_6, paving the way for further investigations into the electronic properties of the broader 166 kagome family, including recently discovered vanadium- and titanium-based kagome compounds.

ACKNOWLEDGMENTS

The work at West Texas A&M University (WTAMU) is supported by the Killgore Undergraduate and Graduate Student Research Grants, the Welch Foundation (Grant No. AE-0025), and the National Science Foundation (Award No. 2336011). DFT calculations were performed in the WTAMU HPC cluster, which was funded by the National Science Foundation (NSF CC* GROWTH 2018841). W.R.M, R.P.M., S.M., and D.G.M. acknowledge the support from AFOSR MURI Grant No. FA9550-20-1-0322 and from the Gordon and Betty Moore Foundation Grant No. GBMF9069 awarded to D.M. L.B. is supported by DOE-BES through Award No. DE-SC0002613. A portion of this work was performed at the National High Magnetic Field Laboratory, which is supported by National Science Foundation Cooperative Agreement No. DMR-2128556 and the State of Florida.

DATA AVAILABILITY

The data that support the findings of this article are not publicly available. The data are available from the authors upon reasonable request.

[1] J.-X. Yin, B. Lian, and M. Z. Hasan, Topological kagome magnets and superconductors, Nature (London) **612**, 647 (2022).

[2] S. D. Wilson and B. R. Ortiz, AV_3Sb_5 kagome superconductors, Nat. Rev. Mater. **9**, 420 (2024).

[3] Y. Wang, H. Wu, G. T. McCandless, J. Y. Chan, and M. N. Ali, Quantum states and intertwining phases in kagome materials, Nat. Rev. Phys. **5**, 635 (2023).

[4] B. R. Ortiz, L. C. Gomes, J. R. Morey, M. Winiarski, M. Bordelon, J. S. Mangum, I. W. H. Oswald, J. A. Rodriguez-Rivera, J. R. Neilson, S. D. Wilson *et al.*, New kagome prototype materials: discovery of KV_3Sb_5, RbV_3Sb_5, and CsV_3Sb_5, Phys. Rev. Mater. **3**, 094407 (2019).

[5] B. R. Ortiz, S. M. L. Teicher, Y. Hu, J. L. Zuo, P. M. Sarte, E. C. Schueller, A. M. Abeykoon, M. J. Krogstad, S. Rosenkranz, R. Osborn *et al.*, CsV_3Sb_5: A Z_2 topological kagome metal with a superconducting ground state, Phys. Rev. Lett. **125**, 247002 (2020).

[6] K. Shrestha, R. Chapai, B. K. Pokharel, D. Miertschin, T. Nguyen, X. Zhou, D. Y. Chung, M. G. Kanatzidis, J. F. Mitchell, U. Welp *et al.*, Nontrivial fermi surface topology of the kagome superconductor CsV_3Sb_5 probed by de Haas–Van Alphen oscillations, Phys. Rev. B **105**, 024508 (2022).

[7] K. Shrestha, M. Shi, T. Nguyen, D. Miertschin, K. Fan, L. Deng, D. E. Graf, X. Chen, and C.-W. Chu, Fermi surface mapping of the kagome superconductor RbV_3Sb_5 using de Haas-Van Alphen oscillations, Phys. Rev. B **107**, 075120 (2023).

[8] K. Shrestha, M. Shi, B. Regmi, T. Nguyen, D. Miertschin, K. Fan, L. Z. Deng, N. Aryal, S.-G. Kim, D. E. Graf *et al.*, High quantum oscillation frequencies and nontrivial topology in kagome superconductor KV_3Sb_5 probed by torque magnetometry up to 45 T, Phys. Rev. B **107**, 155128 (2023).

[9] S. R. Bhandari, M. Zeeshan, V. Gusain, K. Shrestha, and D. Rai, First-principles study of the electronic structure, Z_2 invariant, and quantum oscillation in the kagome material CsV_3Sb_5, APL Quantum **1**, 046118 (2024).

[10] Z. Liang, X. Hou, F. Zhang, W. Ma, P. Wu, Z. Zhang, F. Yu, J.-J. Ying, K. Jiang, L. Shan *et al.*, Three-dimensional charge density wave and surface-dependent vortex-core states in a kagome superconductor CsV_3Sb_5, Phys. Rev. X **11**, 031026 (2021).

[11] W. Zhang, L. Wang, C. W. Tsang, X. Liu, J. Xie, W. C. Yu, K. T. Lai, and S. K. Goh, Emergence of large quantum oscillation frequencies in thin flakes of the kagome superconductor CsV_3Sb_5, Phys. Rev. B **106**, 195103 (2022).

[12] D. Chen, B. He, M. Yao, Y. Pan, H. Lin, W. Schnelle, Y. Sun, J. Gooth, L. Taillefer, and C. Felser, Anomalous thermoelectric effects and quantum oscillations in the Kagome metal CsV_3Sb_5, Phys. Rev. B **105**, L201109 (2022).

[13] C. Broyles, D. Graf, H. Yang, X. Dong, H. Gao, and S. Ran, Effect of the interlayer ordering on the fermi surface of kagome superconductor CsV_3Sb_5 revealed by quantum oscillations, Phys. Rev. Lett. **129**, 157001 (2022).

[14] Z. Wang, W. Zhang, L. Wang, T. F. Poon, C. W. Tsang, W. Wang, J. Xie, S. T. Lam, X. Zhou, Y. Zhao *et al.*, Similarities and differences in the fermiology of kagome metals AV_3Sb_5 (A = K, Rb, Cs) revealed by shubnikov–de haas oscillations, Appl. Phys. Lett. **123**, 012601 (2023).

[15] C. Phillips, K. Shtefiienko, T. Nguyen, A. N. Capa Salinas, B. A. Magar, G. Pokharel, S. D. Wilson, D. E. Graf, and K. Shrestha, Fermi surface reconstruction under pressure in the kagome metal CsV_3Sb_5, Phys. Rev. B **110**, 205135 (2024).

[16] G. Pokharel, S. M. L. Teicher, B. R. Ortiz, P. M. Sarte, G. Wu, S. Peng, J. He, R. Seshadri, and S. D. Wilson, Electronic properties of the topological kagome metals YV_6Sn_6 and GdV_6Sn_6, Phys. Rev. B **104**, 235139 (2021).

[17] J. Lee and E. Mun, Anisotropic magnetic property of single crystals RV_6Sn_6 (R = Y, Gd-Tm, Lu), Phys. Rev. Mater. **6**, 083401 (2022).

[18] S. Peng, Y. Han, G. Pokharel, J. Shen, Z. Li, M. Hashimoto, D. Lu, B. R. Ortiz, Y. Luo, H. Li *et al.*, Realizing kagome band structure in two-dimensional kagome surface states of RV_6Sn_6 (R = Gd, Ho), Phys. Rev. Lett. **127**, 266401 (2021).

[19] E. Rosenberg, J. M. DeStefano, Y. Guo, J. S. Oh, M. Hashimoto, D. Lu, R. J. Birgeneau, Y. Lee, L. Ke, M. Yi *et al.*, Uniaxial ferromagnetism in the kagome metal TbV_6Sn_6, Phys. Rev. B **106**, 115139 (2022).

[20] K. Shrestha, B. Regmi, G. Pokharel, S.-G. Kim, S. D. Wilson, D. E. Graf, B. A. Magar, C. Phillips, and T. Nguyen, Electronic properties of kagome metal ScV_6Sn_6 using high-field torque magnetometry, Phys. Rev. B **108**, 245119 (2023).

[21] Z. Rehfuss, C. Broyles, D. Graf, Y. Li, H. Tan, Z. Zhao, J. Liu, Y. Zhang, X. Dong, H. Yang *et al.*, Quantum oscillations in kagome metals $CsTi_3Bi_5$ and $RbTi_3Bi_5$, Phys. Rev. Mater. **8**, 024003 (2024).

[22] D. Werhahn, B. R. Ortiz, A. K. Hay, S. D. Wilson, R. Seshadri, and D. Johrendt, The kagome metals $CsTi_3Bi_5$ and $RbTi_3Bi_5$, Z. Naturforsch. B **77**, 757 (2022).

[23] B. Liu, M.-Q. Kuang, Y. Luo, Y. Li, C. Hu, J. Liu, Q. Xiao, X. Zheng, L. Huai, S. Peng *et al.*, Tunable van hove singularity without structural instability in kagome metal $CsTi_3Bi_5$, Phys. Rev. Lett. **131**, 026701 (2023).

[24] Y. Hu, X. Wu, Y. Yang, S. Gao, N. C. Plumb, A. P. Schnyder, W. Xie, J. Ma, and M. Shi, Tunable topological dirac surface states and van hove singularities in kagome metal GdV_6Sn_6, Sci. Adv. **8**, eadd2024 (2022).

[25] H. W. S. Arachchige, W. R. Meier, M. Marshall, T. Matsuoka, R. Xue, M. A. McGuire, R. P. Hermann, H. Cao, and D. Mandrus, Charge density wave in kagome lattice intermetallic ScV_6Sn_6, Phys. Rev. Lett. **129**, 216402 (2022).

[26] X. Zhang, J. Hou, W. Xia, Z. Xu, P. Yang, A. Wang, Z. Liu, J. Shen, H. Zhang, X. Dong *et al.*, Destabilization of the charge density wave and the absence of superconductivity in ScV_6Sn_6 under high pressures up to 11 GPa, Materials **15**, 7372 (2022).

[27] X. Dong, Y. Zhang, X. Yi, Z. Zhao, J. Liu, Z. Liu, A. Xu, D. Li, Z. Lu, S. Ma *et al.*, de Haas–van Alphen oscillation reveals nontrivial fermi surface topology in kagome superconductor $CsTi_3Bi_5$, Research Square (2023).

[28] B. R. Ortiz, H. Miao, D. S. Parker, F. Yang, G. D. Samolyuk, E. M. Clements, A. Rajapitamahuni, T. Yilmaz, E. Vescovo, J. Yan *et al.*, Evolution of highly anisotropic magnetism in the titanium-based kagome metals $LnTi_3Bi_4$ (Ln: La Gd^{3+}, Eu^{2+}, Yb^{2+}), Chem. Mater. **35**, 9756 (2023).

[29] B. R. Ortiz, H. Zhang, K. Górnicka, D. S. Parker, G. D. Samolyuk, F. Yang, H. Miao, Q. Lu, R. G. Moore, A. F. May *et al.*, Intricate magnetic landscape in antiferromagnetic kagome metal $TbTi_3Bi_4$ and interplay with $Ln_{2-x}Ti_{6+x}Bi_9$ (Ln: Tb Lu) Shurikagome Metals, Chem. Mater. **36**, 8002 (2024).

[30] K. Shtefiienko, C. Phillips, B. R. Ortiz, D. E. Graf, and K. Shrestha, Electronic structure of the kagome metal $YbTi_3Bi_4$ studied using torque magnetometry, Phys. Rev. B **111**, 035145 (2025).

[31] S. Mozaffari, W. R. Meier, R. P. Madhogaria, N. Peshcherenko, S.-H. Kang, J. W. Villanova, H. W. S. Arachchige, G. Zheng, Y. Zhu, K.-W. Chen *et al.*, Universal sublinear resistivity in vanadium kagome materials hosting charge density waves, Phys. Rev. B **110**, 035135 (2024).

[32] W. R. Meier, R. P. Madhogaria, S. Mozaffari, M. Marshall, D. E. Graf, M. A. McGuire, H. W. S. Arachchige, C. L. Allen, J. Driver, H. Cao *et al.*, Tiny sc allows the chains to rattle: Impact of Lu and Y doping on the charge-density wave in ScV_6Sn_6, J. Am. Chem. Soc. **145**, 20943 (2023).

[33] P. Blaha, K. Schwarz, G. K. Madsen, D. Kvasnicka, J. Luitz *et al.*, wien2k, An augmented plane wave+ local orbitals program for calculating crystal properties, http://www.wien2k.at/reg_user/textbooks/usersguide.pdf.

[34] J. P. Perdew, K. Burke, and M. Ernzerhof, Generalized gradient approximation made simple, Phys. Rev. Lett. **77**, 3865 (1996).

[35] K. Koepernik and H. Eschrig, Full-potential nonorthogonal local-orbital minimum-basis band-structure scheme, Phys. Rev. B **59**, 1743 (1999).

[36] K. Shtefiienko, C. Phillips, S. Mozaffari, R. P. Madhogaria, W. R. Meier, D. G. Mandrus, D. E. Graf, and K. Shrestha, Electronic structure of YV_6Sn_6 probed by de Haas–van Alphen oscillations and density functional theory, APL Quantum **2**, 016118 (2025).

[37] D. Shoenberg, *Magnetic Oscillations in Metals* (Cambridge University Press, New York, 2009).

[38] Y. Ando, Topological insulator materials, J. Phys. Soc. Jpn. **82**, 102001 (2013).

[39] According to the Onsager's relation, the quantum oscillation measured frequency of an electron orbit (F) which is perpendicular to the applied magnetic field is related to the area of the Fermi surface (A) by $F = \frac{\phi_0}{2\pi^2}A$, where $\phi_0 = 2.07 \times 10^{-15}$ T m^2 is the quantum of flux.

[40] See Supplemental Material at http://link.aps.org/supplemental/10.1103/PhysRevB.111.155136 for the angle-dependent Shubnikov–de Haas (SdH) and de Haas–van Alphen (dHvA) oscillations, the frequency analysis, Berry phase calculations, Fermi surface, and effective masses of charge carriers for LuV_6Sn_6.

[41] K. Shrestha, V. Marinova, B. Lorenz, and P. C. Chu, Shubnikov–de Haas oscillations from topological surface states of metallic $Bi_2Se_{2.1}Te_{0.9}$, Phys. Rev. B **90**, 241111(R) (2014).

[42] K. Shrestha, V. Marinova, D. Graf, B. Lorenz, and C. W. Chu, Quantum oscillations in metallic Sb_2Te_2Se topological insulator, Phys. Rev. B **95**, 075102 (2017).

[43] D. Miertschin, T. Nguyen, S. R. Bhandari, K. Shtefiienko, C. Phillips, B. A. Magar, R. Sankar, D. E. Graf, and K. Shrestha, Anisotropic quantum transport in ZrSiS probed by high-field torque magnetometry, Phys. Rev. B **110**, 085140 (2024).

[44] T. Nguyen, N. Aryal, B. K. Pokharel, L. Harnagea, D. Mierstchin, D. Popović, D. E. Graf, and K. Shrestha, Fermiology of the dirac type-ii semimetal candidates (Ni, Zr)Te_2 using de Haas–van Alphen oscillations, Phys. Rev. B **106**, 075154 (2022).

[45] G. Zheng, Y. Zhu, S. Mozaffari, N. Mao, K.-W. Chen, K. Jenkins, D. Zhang, A. Chan, H. W. S. Arachchige, R. P. Madhogaria *et al.*, Quantum oscillations evidence for topological bands in kagome metal ScV_6Sn_6, J. Phys.: Condens. Matter **36**, 215501 (2024).

[46] E. Rosenberg, J. M. DeStefano, Y. Lee, C. Hu, Y. Shi, D. Graf, S. M. Benjamin, L. Ke, and J.-H. Chu, Probing the van hove singularity of the kagome metal YV_6Sn_6 through quantum oscillations, Phys. Rev. B **110**, 035119 (2024).

[47] C. Phillips, G. Pokharel, K. Shtefiienko, S. R. Bhandari, D. E. Graf, D. P. Rai, and K. Shrestha, Electronic structure of the altermagnet candidate $FeSb_2$: High-field torque magnetometry and density functional theory studies, Phys. Rev. B **111**, 075141 (2025).

[48] D. Miertschin, T. Nguyen, S. Zhang, M. Lee, S. Krishnamoorthi, R. K. Ulaganathan, R. Sankar, D. E. Graf, and K. Shrestha, The dhva effect in Sn-doped PbTe topological crystalline insulator, J. Phys.: Condens. Matter **37**, 155501 (2025).

[49] P. M. C. Rourke, Numerical extraction of de Haas–van Alphen frequencies from calculated band energies, Comput. Phys. Commun. **183**, 324 (2012).